

Full length article

Reversed compressive yield anisotropy in magnesium with microlaminated structure

Xin Wang^a, Lin Jiang^a, Dalong Zhang^a, Irene J. Beyerlein^b, Subhash Mahajan^c, Timothy J. Rupert^{a,d}, Enrique J. Lavernia^a, Julie M. Schoenung^{a,*}

^a Department of Chemical Engineering and Materials Science, University of California-Irvine, CA 92697-2575, USA

^b Mechanical Engineering Department, Materials Department, University of California-Santa Barbara, CA 93106, USA

^c Department of Materials Science and Engineering, University of California-Davis, Davis, CA 95616, USA

^d Department of Mechanical and Aerospace Engineering, University of California-Irvine, Irvine, CA 92697, USA



ARTICLE INFO

Article history:

Received 20 September 2017

Received in revised form

10 December 2017

Accepted 10 December 2017

Available online 21 December 2017

Keywords:

Magnesium

Microlaminated structure

Yield anisotropy

Dislocations

Twinning

ABSTRACT

To investigate the effect of grain morphology on the mechanical properties of polycrystalline Mg, two types of bulk Mg samples with equiaxed and microlaminated grain structures were fabricated by spark plasma sintering (SPS) of as-received Mg powder and cryomilled disc-shaped Mg powder particles, respectively. Based on a detailed microstructural investigation, the mechanisms by which microstructure evolves and texture development occurs were identified and are discussed. The basal fiber textures in the SPS consolidated samples allow the plastic anisotropy in such textured Mg to be investigated. Compression tests at room temperature parallel and perpendicular to the SPS compaction axis determined that, in comparison to the conventional anisotropy observed in the equiaxed sample, the anisotropy of yield strength is reversed in the microlaminated sample, with the yield strength for c-axis extension being higher than that for c-axis contraction. The reversed compressive yield strength anisotropy observed in the sample that was cryomilled is related to the low twinning activity, limited twinning growth and the anisotropy induced by the microlaminated grain structure, which offers an opportunity to reduce or even reverse the intrinsic plastic anisotropy of hexagonal close packed Mg.

© 2017 Acta Materialia Inc. Published by Elsevier Ltd. All rights reserved.

1. Introduction

Magnesium (Mg) and its alloys are attractive lightweight structural materials for the automotive and aerospace industries, where specific strength is of significant concern [1,2]. Unlike metals with cubic crystal structures, Mg, which has a hexagonal close packed (HCP) crystal structure, is subject to slip on multiple nonequivalent slip systems upon plastic deformation. The slip systems that have been reported for Mg are slip in the $a/3\langle 11\bar{2}0 \rangle$ (or $\langle a \rangle$) directions on the basal, prismatic and pyramidal planes, and slip in the $a/3\langle \bar{2}113 \rangle$ (or $\langle c + a \rangle$) directions on the pyramidal planes [3,4]. Unfortunately, the critical resolved shear stresses (CRSSs) vary significantly for different slip systems [3,4]. The ratio of the CRSS value for non-basal slip to that for basal slip lies in the range of 40–100 in single crystal Mg and in the range of 2.0–13.5 in polycrystalline Mg [3]. The much lower CRSS value for

basal slip renders slip on non-basal planes difficult to initiate. Basal slip alone, however, only provides two independent slip modes, which are insufficient for homogeneous deformation of a polycrystalline material according to the von Mises criterion [5]. Extension twins of the $\{10\bar{1}2\}\langle 10\bar{1}1 \rangle$ type (hereafter referred to as $\{10\bar{1}2\}$ twins) are easily activated in Mg when loaded in tension along the c-axis or in compression perpendicular to the c-axis. HCP twins can provide an additional deformation mechanism despite the fact that twinning is polar in nature and that the maximum twinning-induced plastic strain is recognized to be limited [4]. As a result of the anisotropy in slip and twinning discussed above, strong deformation textures are common in wrought Mg [6–8], which lead to a plastically anisotropic stress-strain response [9]. This plastic anisotropy complicates the processing of Mg alloys, which limits their use in many important structural applications despite the obvious density advantages.

In an effort to circumvent the limitations that originate from the plastic anisotropy that is inherent to Mg and its alloys, various approaches have been proposed. For example, texture modification,

* Corresponding author.

E-mail address: julie.schoenung@uci.edu (J.M. Schoenung).

through addition of rare earth elements [10,11], and careful selection of thermo-mechanical processing parameters [12–14], have been successfully demonstrated to reduce the plastic anisotropy and enhance the ductility of Mg. In addition to weakening the initial texture, rare earth elements can promote non-basal slip activity by significantly decreasing the critical stress required for cross-slip stress [10,15]. The drawback of this method, however, is the high cost of rare earth elements, which limits large scale application of these alloy compositions. In addition to rare earth alloying, decreasing the grain or sample size is a promising strategy to reduce the plastic anisotropy of Mg by inhibiting twinning [16,17] and reducing the CRSS ratio between non-basal and basal slip [18]. Dislocation density also influences the CRSS ratio in Mg [3]. With a dislocation density increased from $\sim 10^6$ to $\sim 10^{14} \text{ m}^{-2}$, the CRSS ratio between prismatic to basal slip in Mg can be reduced from 40:1 to as low as $\sim 2:1$ [3]. Interestingly, review of the published literature shows that despite numerous studies that address various microstructural factors, the influence of grain morphology on the deformation, particularly on the plastic anisotropy, of Mg has not been addressed, which provided a motivation for the current study.

To synthesize Mg with distinct non-equiaxed grain morphology, mechanical milling was used in the present work. Mechanical milling is a powder-based severe plastic deformation material processing method that can be used to synthesize fine-grained or nanocrystalline materials in relatively large quantities [19,20]. As such, mechanical milling techniques have been used to study a broad range of materials and have been successfully used in combination with various consolidation approaches to attain notable properties in various metals, alloys and composites [19–21]. Of interest is that, in some studies, mechanical milling has been used to fabricate disc-shaped powders, which facilitate consolidation into laminated composites with enhanced mechanical performance [22–25]. Of perhaps more interest here is a recent finding of an orientation-dependent strengthening effect in nanolaminated graphene-Al composites, where the highest compressive strength was observed when the lamellae were oriented parallel to the compression axis [25]. In view of the published literature, mechanical milling followed by subsequent sintering has been observed in a few studies to improve the mechanical properties, particularly the strength and hardness, of Mg alloys through grain refinement [26,27]. However, none of these studies have reported on the yield anisotropy of materials processed by this method. Moreover, the microstructure of these materials has not been studied in detail and information related to texture, dislocation configurations and grain boundary characteristics is not currently available.

In the present work, we demonstrate that the plastic anisotropy for Mg can be altered through microstructural design, such as through changes in the grain morphology and dislocation structure without alloying. For this purpose, the texture and microstructure of a microlaminated Mg structure, created by spark plasma sintering (SPS) consolidation of disc-shaped powder particles obtained by cryomilling, was comparatively studied together with a sample that was not cryomilled prior to sintering. We used scanning electron microscopy (SEM), X-ray diffraction (XRD), electron backscattered diffraction (EBSD) and transmission electron microscopy (TEM) to probe the microstructural and texture development in powder particles during cryomilling and sintered bulk samples. Uniaxial compression tests were performed on bulk samples. Notably, an uncommon compressive yield anisotropy was observed in the samples that was cryomilled, which sheds light on the possibility of reducing the plastic anisotropy in Mg through microstructural design.

2. Experimental

The starting material used in this study was a commercially pure Mg powder (99.8% purity, 325 mesh, Alfa Aesar, Massachusetts, United States). One kg of as-received powder (hereafter referred to as AR-Mg) was attrition ball milled in liquid argon at a speed of 180 rpm with a stainless steel ball-to-powder mass ratio of 30:1. Powder samples were collected after a 1, 2, 4, 6 and 8 h milling time (hereafter referred to as 1 h-Mg, 2 h-Mg, 4 h-Mg, 6 h-Mg and 8 h-Mg, respectively). To prevent excessive cold welding, $\sim 0.5 \text{ wt}\%$ of stearic acid was added to the powders as a process control agent.

As-milled Mg powders were packed into a double-acting die arrangement, which is schematically illustrated in Fig. 1. SPS was applied to prepare bulk Mg samples. In all cases, Mg powders were handled in an argon-filled glove box and transferred to the SPS chamber directly to minimize oxidation reactions. SPS was carried out using a DR. SINTER SPS-825 S (Syntex Inc., Kawasaki, Japan) under vacuum to produce a cylinder-shaped bulk sample, typically 5 mm in diameter and 5 mm in height. A 200 MPa uniaxial sintering pressure and a fast heating rate of $\sim 100 \text{ }^\circ\text{C}/\text{min}$ was achieved with this SPS apparatus and die set. The sintering parameters are summarized in Table 1. The use of a fast heating rate and a low sintering temperature were intended to limit grain growth during powder consolidation. For comparison purposes, as-received (i.e., unmilled AR-Mg) powder was also sintered using identical SPS conditions.

SEM microstructural analysis was performed on an FEI XL30 SFEG SEM. XRD measurements were carried out with a Scintag XDS2000 using Cu K_α ($\lambda = 0.1542 \text{ nm}$) radiation at a step size of 0.02° with a dwell time of 2 s per step from 20 to 80° . To prepare samples for EBSD, the SPS consolidated bulk samples were sectioned using a diamond wire-saw in a way that the viewing plane was parallel to the SPS compaction axis (CA) at the center of the cylindrical sample. The cut surface was ion-polished by a cross-section polisher (JEOL, Model SM-09010). EBSD analysis was performed utilizing an FEI Scios SEM equipped with an Oxford Instruments EBSD detector. The voltage and beam current used for EBSD data collection were 30 kV and 13 nA, respectively.

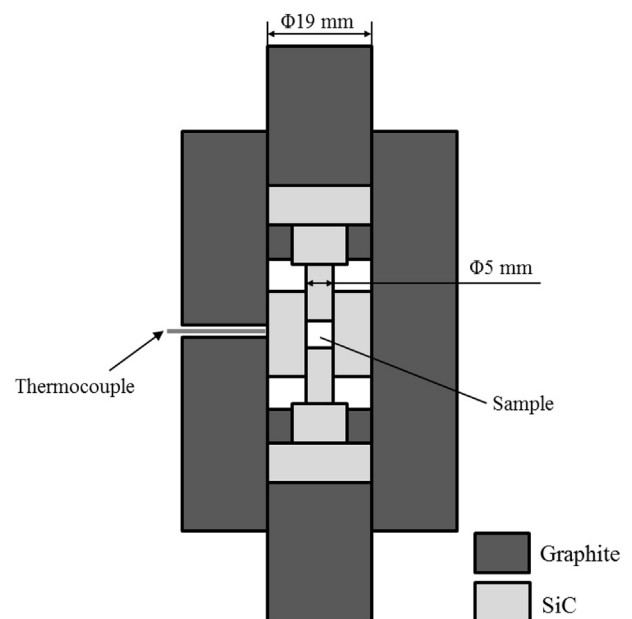


Fig. 1. A schematic of the double-acting die setup for SPS.

Table 1
The SPS parameters.

Pressure (MPa)	200
Heating rate (°C/min)	107
Holding temperature (°C)	390
Dwell time (min)	3
Pulse on/off time ratio	6:1
Starting vacuum (Pa)	<1

The step size for EBSD data collection was 0.75–1 μm . EBSD post-processing was carried out using Channel 5 system from HKL Technology. TEM microstructural analysis of the as-milled Mg powders and SPS consolidated bulk samples was performed using a JEOL 2500 or PHILIPS/FEI CM 20 operating at 200 kV. To prepare TEM samples from the cryomilled powders, the powders were mixed with G-1 epoxy (Gatan) and cured at room temperature to form a disk. The powder-epoxy mixture was mechanically polished and ion-milled (dual ion-beam Gatan PIPS). The sintered Mg samples were sectioned parallel to the SPS CA, and then thinned by the same polishing-ion-milling method.

Compression samples were electrical discharge machined into 3 mm cubes. Uniaxial compression tests were performed at room temperature using an Instron 8801 universal testing machine, parallel and perpendicular to the SPS compaction axis (CA). A displacement-controlled mode with an initial strain rate of 10^{-3} s^{-1} was employed in this study. Some of the compression tests were interrupted and a subsequent EBSD analysis was performed.

3. Results

3.1. Evolution of powder particle morphology and microstructure during cryomilling

Fig. 2 displays secondary electron SEM micrographs of the as-received powder particles and powder particles subjected to increasing cryomilling time of 1–8 h to reveal the evolution in powder morphology. The as-received Mg powder particles (Fig. 2 (a)) are slightly oblong in shape and mostly from 10 to 80 μm in diameter with an average particle size of $\sim 30 \mu\text{m}$. After up to 2 h of cryomilling, (Fig. 2 (b) and (c)), the powder particles were flattened into disc-shaped powder particles $\sim 90 \mu\text{m}$ in diameter and $\sim 1 \mu\text{m}$ in thickness. When the milling time was further increased to 4 and to 6 h (Fig. 2 (d) and (e)), non-uniform agglomerates formed as a result of impact-induced fracture of disc-shaped powder particles and random cold welding among particles. Finally, at 8 h, when a dynamic balance between particle fracture and cold welding was attained, nearly equiaxed faceted particles with a uniform particle size of $\sim 17 \mu\text{m}$ were obtained (Fig. 2 (f)).

XRD patterns for the Mg powders as a function of cryomilling time (Fig. 3) confirmed that all powders had an HCP structure with lattice parameters matching with JCPDS #35–0821 for pure Mg. Moreover, the relative integrated intensities of XRD peaks indicated the preferential orientations in the as-milled powder particles. The $I_{(0002)}/I_{(10-10)}$ integrated intensity ratio for the starting material is ~ 1.3 , which is similar to 1.4 for the reference pattern, indicating a random crystalline orientation in the as-received powder. As cryomilling progresses, a gradual growth in the relative intensity of (0002) peaks can be observed in 1 h-Mg and 2 h-Mg. After 2 h of

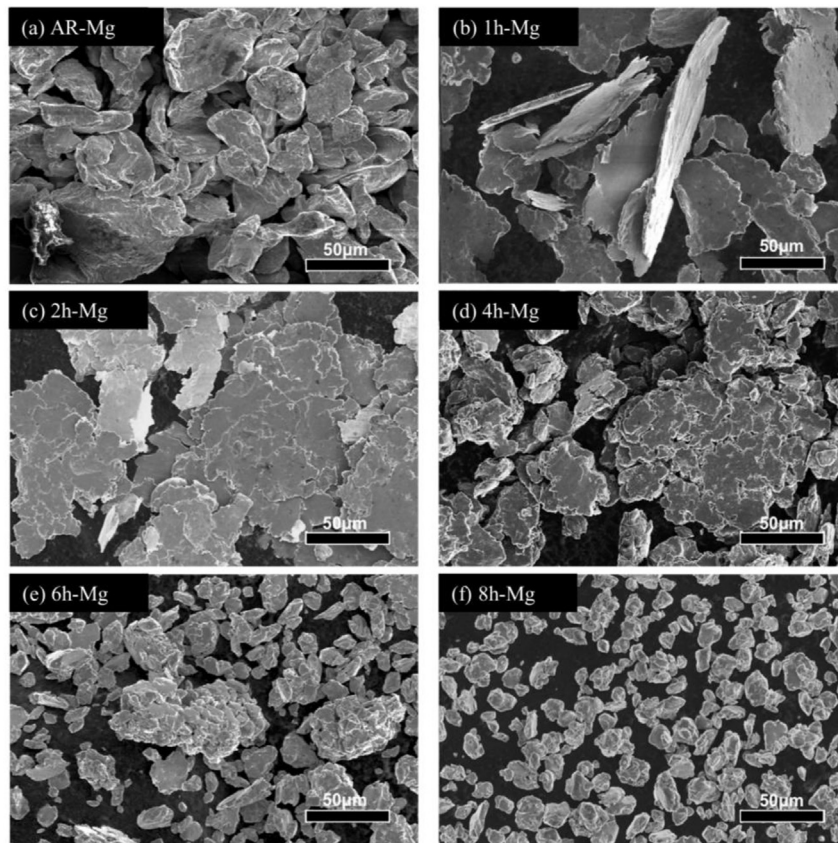


Fig. 2. SEM micrographs of: (a) as-received Mg powders and cryomilled powders collected after (b) 1 h, (c) 2 h, (d) 4 h, (e) 6 h and (f) 8 h milling time.

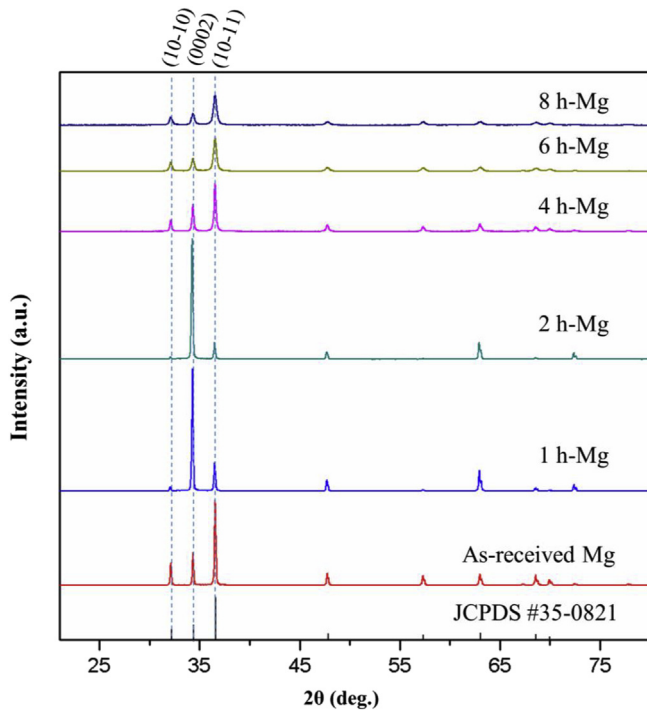


Fig. 3. XRD patterns of as-received and cryomilled magnesium powder particles.

cryomilling, the (0002) peak showed the highest $I_{(0002)}/I_{(10-10)}$ intensity ratio of ~ 58.8 , suggesting the predominance of (0002) planes parallel to the diffracting flat-on surfaces of the lamellae. When the cryomilling time was increased to 4 h, the (0002) peak intensity started to decline, and concomitantly losing the particle shape anisotropy, as observed in Fig. 2 (d). The $I_{(0002)}/I_{(10-10)}$ intensity ratio dropped back to ~ 1.4 in 8 h-Mg.

The multiple whole profile (MWP) fitting program developed by Ungar et al. [28] was used to estimate the dislocation density in the cryomilled Mg powder particles. As seen in Table 2, the measured dislocation density first increased and reached a maximum of $\sim 9.10 \times 10^{15} \text{ m}^{-2}$ in 2 h-Mg, when mostly basal planes were diffracting. The measured dislocation density then decreased when the milling time reached 4 h, and increased again between 6 h-Mg and 8 h-Mg. The high dislocation densities in the cryomilled powders suggest recrystallization is largely suppressed by the cryogenic liquid argon temperature. Furthermore, the XRD predicted dislocation densities in the cryomilled powders first increased and then decreased after 4 h. This trend agrees with that observed for the extent of basal planes being parallel to the lamellar flat-on surfaces, suggesting a higher dislocation density on the basal planes relative to the non-basal planes.

To further substantiate the above assessment, TEM analysis was performed on cryomilled 2 h-Mg powder particles, which exhibited the highest dislocation density and the highest XRD peak intensity ratio (i.e., orientation preference). Composite bright-field TEM micrographs in Fig. 4 (a) show the cross section of a representative 2 h-Mg lamellar particle embedded in the G1 epoxy matrix. The

particle is $\sim 1.1 \mu\text{m}$ in thickness and consists of several elongated grains along the lamellar band direction, separated by nearly vertical grain boundaries. Fig. 4 (b) and (c) are bright field micrographs taken at the same region under the two-beam conditions with diffraction vectors $\mathbf{g} = 01-11$ and $\mathbf{g} = 0002$, respectively, near the $[2-1-10]$ Mg zone axis. According to the $\mathbf{g} \cdot \mathbf{b} = 0$ criterion, when $\mathbf{g} = 01-11$ was used, all types of dislocations ($\langle \mathbf{a} \rangle$, $\langle \mathbf{c} \rangle$ and $\langle \mathbf{c} + \mathbf{a} \rangle$) can be observed; whereas, if the $\mathbf{g} = 0002$ is used, only $\langle \mathbf{c} \rangle$ or $\langle \mathbf{c} + \mathbf{a} \rangle$ dislocations can be seen. A high density of dislocations is present in 2 h-Mg when $\mathbf{g} = 01-11$, while most dislocations are not visible when $\mathbf{g} = 0002$. Moreover, most dislocation lines in Fig. 4 (b) are parallel to the basal plane trace, which is nearly parallel to the lamellar band, as highlighted by the yellow dashed line. This alignment confirms that the observed dislocations are mostly basal $\langle \mathbf{a} \rangle$ dislocations. Several non-basal $\langle \mathbf{a} \rangle$ dislocations not parallel to the basal plane trace are also seen, as highlighted by the red arrows in Fig. 4 (b). In summary, TEM confirms that dislocations in 2 h-Mg are predominantly basal $\langle \mathbf{a} \rangle$ dislocations, with a moderate density of non-basal dislocations.

3.2. Microstructure and texture of as-sintered Mg bulk samples

To examine the role of grain morphology during SPS processing, AR-Mg and 2 h-Mg powder particles were sintered using identical pressure-assisted SPS conditions to produce bulk samples, hereafter referred to as AR-Mg-SPS and 2 h-Mg-SPS, respectively. The 2 h-Mg powder was selected for consolidation and subsequent characterization due to its extreme grain morphology anisotropy and high dislocation density. The 8 h-Mg powder was also consolidated, but retained equiaxed nanometric grains after both cryomilling and consolidation, thus making characterization of the consolidated material beyond the scope of the current study. Findings on the 8 h-Mg-SPS sample will be explored in detail in future work.

Fig. 5 shows the EBSD inverse pole figure (IPF) maps, color-coded with respect to the SPS CA (vertical direction in the maps), for AR-Mg-SPS and 2 h-Mg-SPS, together with the corresponding grain size area fraction histograms. In the IPF maps, high angle grain boundaries (HAGBs) with misorientation angles larger than 15° are colored in black, and low angle grain boundaries (LAGBs) with misorientation angles between 2° and 15° are colored in grey. As shown in Fig. 5 (a), clusters of small equiaxed grains in a “necklace”-type arrangement surrounding the coarse grains can be observed from the IPF map. The grain size statistics in Fig. 5 (c), calculated from the EBSD map, indicate a nearly bimodal grain size distribution with grain diameter ranging from less than $1 \mu\text{m}$ to larger than $37 \mu\text{m}$. The average grain size of AR-Mg-SPS is $\sim 13.2 \mu\text{m}$. The IPF map for 2 h-Mg-SPS in Fig. 5 (b) reveals a refined grain structure. Originating from the 2 h-Mg disc-shaped powder particles, a lamellar band structure can be viewed in this sample. Similar laminated structures are characteristic of high-strain rolled or extruded metals [29,30], but compared to the laminated microstructure produced by rolling or extrusion, the lamellar bands in 2 h-Mg-SPS are less straight and less parallel. Each band contains multiple elongated grains. Dark regions in this IPF map are areas that cannot be indexed by EBSD, due to the small grain sizes and/or high strains in these locations. A narrower grain size distribution

Table 2
Dislocation densities of Mg powder particles after different cryomilling times.

Milling time (h)	1	2	4	6	8
Dislocation density ($1/\text{m}^2$)	9.54×10^{14}	9.10×10^{15}	9.55×10^{14}	5.25×10^{14}	8.69×10^{14}

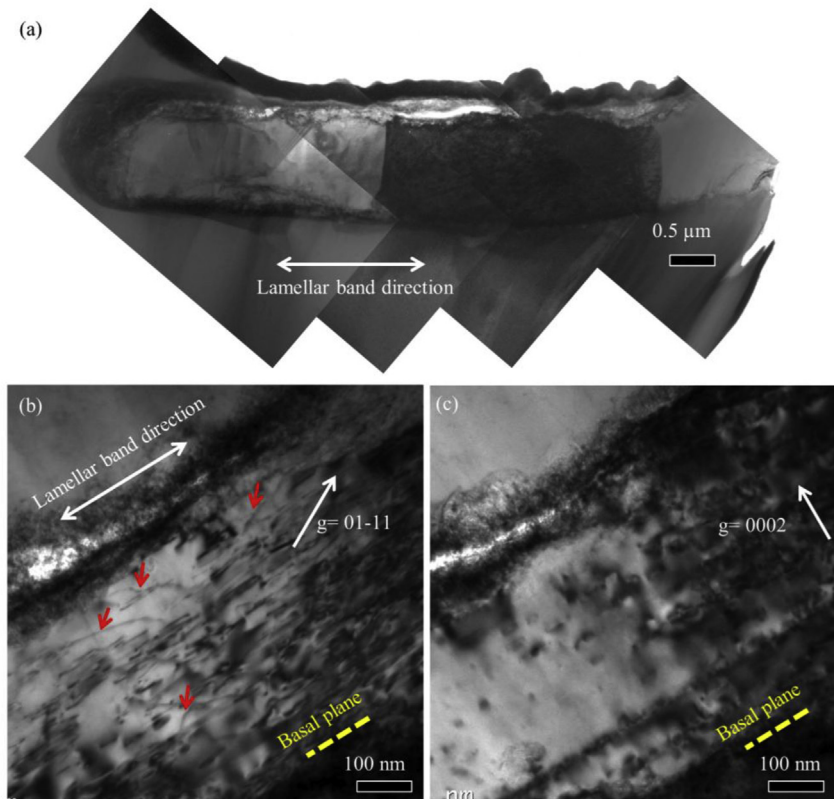


Fig. 4. TEM images of cryomilled 2 h-Mg powder particles: (a) composite low magnification bright field image showing the structure of an as-milled lamellar particle; (b) $g = 01-11$ two-beam bright field image near $[2-1-10]$ zone axis showing all types of dislocations; (c) $g = 0002$ two-beam bright field image showing only $\langle c \rangle$ or $\langle c + a \rangle$ dislocations.

range is found for 2 h-Mg-SPS, giving an average grain size of $\sim 6.6 \mu\text{m}$. To reveal the grain sizes of laminated grains in the two perpendicular directions of interest, i.e., the directions parallel and perpendicular to the SPS CA, linear intercept grain sizes were calculated for 2 h-Mg-SPS along the vertical and horizontal directions using the EBSD map in Fig. 5 (b). The distributions of the horizontally and vertically linear intercept grain sizes are plotted in Fig. 5 (e) and (f), respectively. The average intercept grain size is $\sim 2.8 \mu\text{m}$ for the vertical direction and $\sim 8.0 \mu\text{m}$ for the horizontal direction, which quantifies the average lamellar thickness and length, respectively.

Despite the differences in the processing and morphologies of the two feedstock powder particles, both as-sintered samples developed non-random crystal orientations. As visualized from the IPF maps in Fig. 5, most grains in the sintered samples have their c -axes close to the SPS CA, as represented by the red grain color. The (0001) and (10-10) pole figures, and the inverse pole figures from the SPS CA for AR-Mg-SPS and 2 h-Mg-SPS, respectively, are displayed in Fig. 6 (a) and (b). From the pole figures and inverse pole figures, a basal fiber texture, i.e., with the basal poles aligned along the SPS CA, can be identified in both samples, and the intensities of the basal poles are nearly radial symmetric around the SPS CA. Peak texture intensities in units of m.u.d. (multiples of uniform density) are indicated. Compared to AR-Mg-SPS, 2 h-Mg-SPS has a higher peak intensity in the basal pole figures and a narrower angular spread of basal poles from the SPS CA. Similar strong textures are often observed in pure Mg or dilute Mg alloys after conventional rolling [31–33].

The microstructure and dislocation structures of the 2 h-Mg-SPS sample were further examined by TEM. As shown in the bright field image in Fig. 7 (a), the microstructure of 2 h-Mg-SPS is

characterized by near horizontal lamellar bands, that are perpendicular to the SPS CA. Based on sampling over ~ 100 bands, the majority of lamellar thicknesses range from 0.5 to $3 \mu\text{m}$. A representative two-beam bright field image near the $[2-1-10]$ zone axis, with diffraction vector $g = 01-1-1$, is shown in Fig. 7 (b). $\langle a \rangle$ type dislocations parallel to the trace of the basal plane are dominant similar to that in the 2 h-Mg powder. Moreover, the cross slip of $\langle a \rangle$ dislocations between basal and prismatic/pyramidal planes is observed, as indicated by the red arrows. Since the stacking fault energy (SFE) on the basal planes in Mg is much lower than that on the non-basal planes [34], the cross slip observed here is more likely cross slip from prismatic/pyramidal planes to basal planes. A dislocation wall structure is also seen in this grain, as indicated by the black dashed lines. Low angle grain boundaries in the form of dislocation cells have been reported as a result of dislocation interactions and rearrangement during recovery [35], Fig. 7 (c) and (d) are two-beam dark field images of another sample region under $g = 01-10$ and $g = 0002$ conditions, respectively, near $[2-1-10]$ zone axis. Most $\langle a \rangle$ type dislocations in Fig. 7 (c) are parallel to the basal plane trace, whereas some others are out of the basal plane, as highlighted with red arrows. A much lower density of $\langle c \rangle$ or $\langle c + a \rangle$ dislocations, as compared to $\langle a \rangle$ type dislocations, are present in Fig. 7 (d), and they tend to align with the trace of the basal plane. Therefore, the dislocations in 2 h-Mg-SPS consist of a high density of basal $\langle a \rangle$ dislocations and some non-basal dislocations, with some being non-basal $\langle a \rangle$ dislocations, and others being $\langle c \rangle$ or $\langle c + a \rangle$ dislocations.

3.3. Grain boundary misorientation analysis

Correlated misorientation (i.e., misorientation at grain

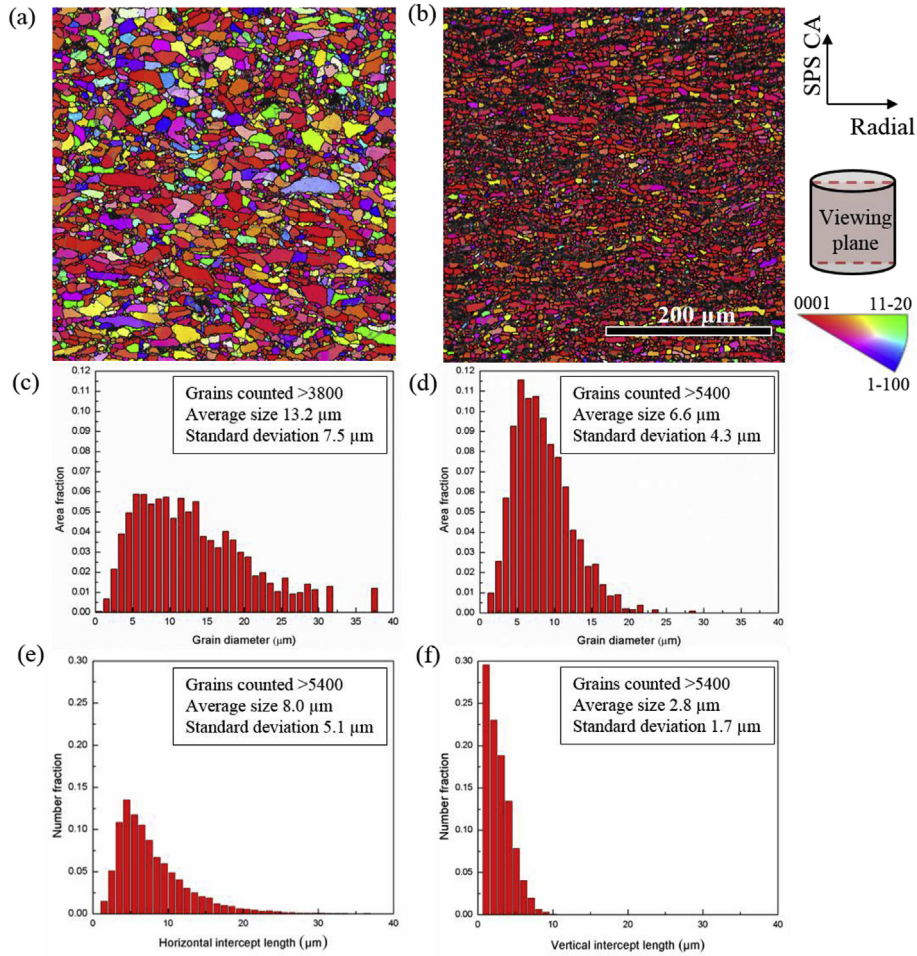


Fig. 5. EBSD microstructural analysis of SPS sintered Mg samples: (a) and (b) are the inverse pole figure (IPF) colored maps along the SPS compaction axis (CA) of AR-Mg-SPS and 2 h-Mg-SPS, respectively. High angle grain boundaries with misorientations $>15^\circ$ are colored in black and small angle grain boundaries with 2° – 15° misorientations are colored in grey; (c) and (d) are the grain size distributions corresponding to (a) and (b), respectively; (e) and (f) are the linear intercept grain size distributions for 2 h-Mg-SPS along the horizontal and vertical directions, respectively.

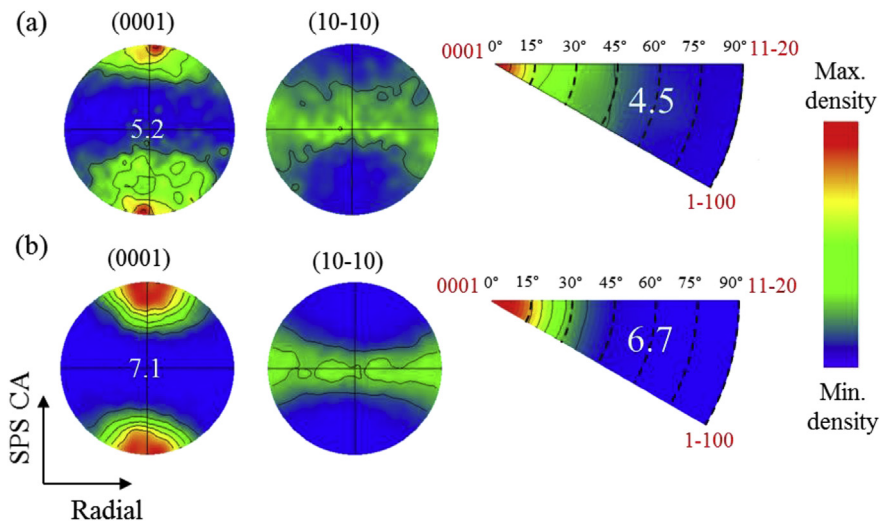


Fig. 6. (0001) and (10-10) pole figures and inverse pole figures along the SPS compaction axis (CA) for: (a) AR-Mg-SPS and (b) 2 h-Mg-SPS.

boundaries) distributions (with a 2° lower threshold) are plotted in Fig. 8 (a) and (b) for AR-Mg-SPS and 2 h-Mg-SPS, respectively. A strong frequency peak in the 2° – 15° low-angle grain

boundaries (LAGBs) regime can be identified in both samples. In the $>15^\circ$ high-angle grain boundaries (HAGBs) regime, the distribution exhibits a broad peak in AR-Mg-SPS, while a

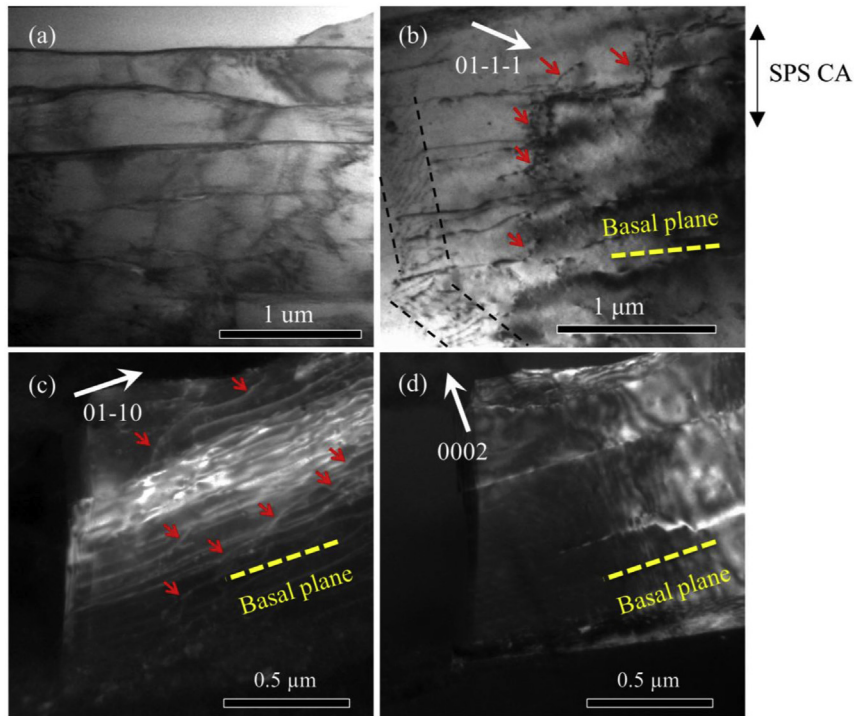


Fig. 7. TEM micrographs of 2 h-Mg-SPS: (a) is a bright field cross-sectional TEM images showing the typical lamellar band structure; (b) is a two-beam bright field image under $g = 01-1-1$ near $[2-1-10]$ zone axis; (c) and (d) are two beam dark field images at the same region under $g = 01-10$ and $g = 0002$, respectively, near $[2-1-10]$ zone axis.

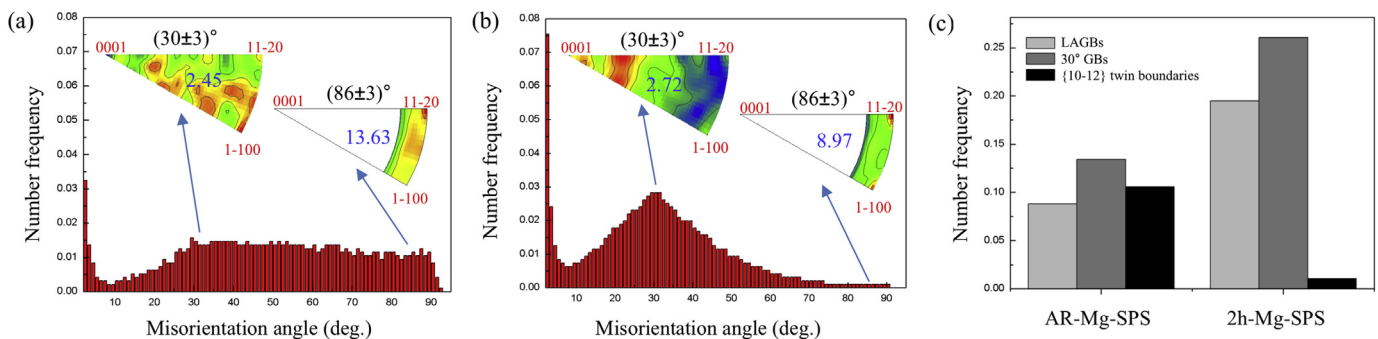


Fig. 8. (a) and (b) are the correlated misorientation angle distributions obtained from the EBSD data for AR-Mg-SPS and 2 h-Mg-SPS, respectively. Insets are the misorientation axis distributions for two angular ranges of interest; (c) shows a comparison of the frequencies of low angle grain boundaries (LAGBs), $\sim 30^\circ$ grain boundaries and $\{10-12\}$ twin boundaries in AR-Mg-SPS and 2 h-Mg-SPS.

pronounced maxima near 30° are present in 2 h-Mg-SPS. In addition, the AR-Mg-SPS exhibits a detectable frequency peak near 90° , presumably corresponding to the $\sim 86^\circ$ $\{10-12\}$ twins in Mg. However, the population of $\sim 86^\circ$ grain boundaries in 2 h-Mg-SPS is almost negligible, indicating the low occurrence of twins in this sample, which is consistent with our TEM observations in Fig. 4. Furthermore, in the inset of Fig. 8, distributions of rotation axes for misorientation angle ranges of $(30 \pm 3)^\circ$ and $(86 \pm 3)^\circ$ in the SPS sintered samples are plotted in the form of inverse pole figures. The rotation axes for $\sim 30^\circ$ grain boundaries appear random in sample AR-Mg-SPS. In contrast, in sample 2 h-Mg-SPS, the $\sim 30^\circ$ rotation axes are predominantly centered around the c-axis. The high frequency of $30^\circ/[0001]$ grain boundaries most likely corresponds to the recrystallization in HCP metals [12,36]. In addition, the rotation axes for $\sim 86^\circ$ grain boundaries in AR-Mg-SPS are mainly clustered around the $\langle 11-20 \rangle$ direction, consistent with the $\{10-12\}$ twin boundaries with an $86^\circ/$

$\langle 11-20 \rangle$ twin-matrix misorientation relationship. Though the frequency of 86° grain boundaries is low in 2 h-Mg-SPS, clustering of 86° rotation axes around $\langle 11-20 \rangle$ suggests the possible occurrence of $\{10-12\}$ twins within some favorably oriented grains in 2 h-Mg-SPS. The frequencies of the three types of characteristic grain boundaries (LAGBs, $(30 \pm 3)^\circ$ grain boundaries, and $(86 \pm 3)^\circ$ $\{10-12\}$ twin boundaries) in the two SPS sintered samples are compared in Fig. 8 (c). Though important in Mg deformation, $\{10-11\}$ contraction twins are not plotted here, since the confidence in identifying this type of twin by misorientation angle is considered low, as they are extensively reported to be thin, scarce and hard to detect [35,37]. Moreover, $\{10-11\}$ contraction twins and $\{10-11\}$ - $\{10-12\}$ double twins are favorable sites for recrystallization [28], so they have a high propensity to be consumed by new grains. While the number frequency of LAGBs in AR-Mg-SPS is only $\sim 8.8\%$, the value in 2 h-Mg-SPS is $\sim 19.5\%$. The higher fraction of LAGBs in 2 h-Mg-SPS can

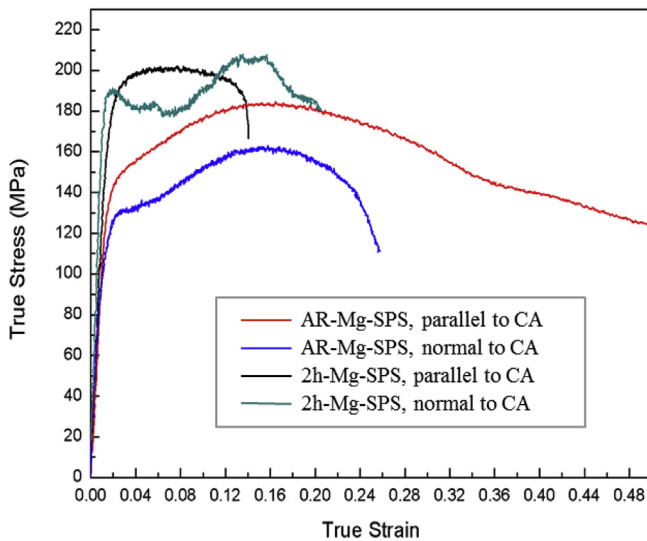


Fig. 9. Compressive true stress-strain curves for AR-Mg-SPS and 2 h-Mg-SPS along directions parallel and normal to SPS CA.

be understood by the high density of dislocations induced by the severe plastic deformation during cryomilling, which tend to rearrange into dislocation cell structures and then convert into LAGBs [38,39]. The fraction of 86° $\{10\text{--}12\}$ twin boundaries (within a $\pm 5^\circ$ misorientation tolerance) in AR-Mg-SPS is $\sim 10.6\%$, compared to $\sim 1.0\%$ in 2 h-Mg-SPS. The frequency of 30° misorientation grain boundaries (within a $\pm 5^\circ$ misorientation tolerance) in 2 h-Mg-SPS ($\sim 26.1\%$) is almost twice that in AR-Mg-SPS ($\sim 13.4\%$).

3.4. Mechanical properties of and anisotropy in SPS consolidated Mg

The loading direction relative to the basal fiber texture and the laminate orientation is expected to influence the deformation behavior. In order to study the mechanical behavior along different orientations, uniaxial compression tests were performed at room temperature both parallel and perpendicular to the SPS CA, corresponding to *c*-axis contraction and *c*-axis extension, respectively, according to the texture measurements. The true stress-strain curves for AR-Mg-SPS and 2 h-Mg-SPS are plotted in Fig. 9, and the compressive strength values are summarized in Table 3. For AR-Mg-SPS compressed along the SPS CA, the 0.2% yield strength and maximum strength are 130 MPa and 183 MPa, respectively. When compressed normal to the SPS CA, a concave shape for the true stress-strain curve is observed, which is typical for twinning-dominated deformation in textured Mg polycrystals; the 0.2% yield strength is 107 MPa, and the maximum strength has a value of 162 MPa. 2 h-Mg-SPS exhibits higher strength than AR-Mg-SPS along both directions. When compressed parallel to the SPS CA, the 0.2% yield strength is 179 MPa, and the maximum strength is measured to be 201 MPa. When the loading direction is normal to the SPS CA, the yield strength and maximum strength are 187 MPa and 205 MPa, respectively. Compared to AR-Mg-SPS, the yield strength of 2 h-Mg-SPS when compressed parallel and normal to the SPS CA increased by 38% and 75%, respectively. Moreover, 2 h-Mg-SPS showed a smaller difference in yield strength values along the two directions than AR-Mg-SPS, despite its stronger basal texture. The possible mechanisms for this unusual behavior are discussed below.

4. Discussion

4.1. Deformation and grain refinement during milling

In the early stage of the milling process the plastic deformation that is induced by ball-powder-ball collisions effectively modifies the powder morphology from equiaxed to disc-like [19,40,41]. In tandem, dislocation nucleation and accumulation and the formation of sub-grain boundaries occur at the microscopic scale [19,40,42,43]. In a well-established model based on metals with cubic crystal structures [19], powders undergo a three-stage process of grain refinement during milling, which include strain localization into narrow shear band zones, annihilation and rearrangement of dislocations to form subgrains, and finally, transformation of LAGBs into HAGBs [19]. Compared to cubic crystals, the poor low-temperature ductility in Mg suggests a much higher probability of powder fracture during cryomilling, leading to a more rapid decrease in the particle size of HCP Mg. This is confirmed by the average particle size of Mg ($\sim 17 \mu\text{m}$), which is significantly smaller than the particle size of, for example, pure Cu ($\sim 34 \mu\text{m}$) or Al 5083 ($\sim 91 \mu\text{m}$) after the same 8 h of cryomilling [27]. Moreover, the microstructural evolution in HCP metals during cryomilling is further complicated by the variety of different slip systems that are active as well as the high propensity for deformation by twinning. Therefore, the mechanisms for grain refinement, particle flattening, as well as the evolution of orientation preference during milling that occur in cubic systems may not be directly applicable to rationalize the evolution of microstructure in Mg during milling.

We provide a schematic diagram (Fig. 10) that illustrates a proposed mechanism to explain the evolution of the structure during cryomilling of Mg. Due to the anisotropic HCP structure with distinct CRSS values associated with different slip systems, the angle between the basal plane and the impact loading direction influences deformation behavior. To explore this relationship in the case of Mg cryomilling, we consider an equiaxed crystal without initial dislocations, with the basal planes oriented at three possible angles (denoted as θ_1 , θ_2 and θ_3 , having values between 0° and 90° as described below) relative to the impact loading axis. First, when θ_1 is approximately 45° (Fig. 10 (a)), a maximized Schmid factor for basal $\langle a \rangle$ slip is expected for this crystal. Basal slip is therefore favorable during the deformation, which will lead to increasing changes in both grain and particle morphology, i.e., elongation perpendicular to the loading axis, as illustrated in Fig. 10 (b). Consequently, although the initial impact loading direction is largely arbitrary, the following impact will have a higher chance to load perpendicular to the elongated surface. Therefore, the angle between the loading axis and the basal planes after the first scenario of impact loading will become larger than θ_1 , and will continue to increase with an accumulation in strain induced during cryomilling.

Second, when θ_2 is close to 0° (Fig. 10 (f)), i.e., the impact loading axis is nearly perpendicular to the *c*-axis, $\{10\text{--}12\}$ twins are favored. $\{10\text{--}12\}$ twins will grow to accommodate the strain along the *c*-axis and will lead to a sharp reorientation of the original crystal by $\sim 86^\circ$. Consequently, the angle between the loading axis and the basal planes after the second scenario of impact loading will be near 90° , as seen in Fig. 10 (g). Despite the fact that $\{10\text{--}12\}$ twinning is favored in this scenario, $\{10\text{--}12\}$ twin boundaries are not detected in 2 h-Mg by TEM (Fig. 4). Possible explanations include: (1) the high impact loading and plastic strain introduced by the milling balls lead to the growth of the $\{10\text{--}12\}$ twins, which can easily consume the entire original matrix. Non-basal $\langle a \rangle$ dislocations, as seen in Fig. 4 (b), can be activated over twinning to accommodate the plastic deformation; (2) although the resolved

Table 3
Compressive strengths of the SPS-consolidated Mg samples parallel or normal to the SPS compaction axis (CA) and the corresponding compressive yield anisotropy ($\sigma_{0.2\%}$ ratio, defined as the ratio of the yield strength for c-contraction to the yield strength for c-extension).

	Compression orientation	$\sigma_{0.2\%}$ (MPa)	σ_{max} (MPa)	$\sigma_{0.2\%}$ ratio (c-contraction/c-extension)
AR-Mg-SPS	parallel to SPS CA (c-axis contraction)	130	183	1.21
	normal to SPS CA (c-axis extension)	107	162	
2 h-Mg-SPS	parallel to SPS CA (c-axis contraction)	179	201	0.96
	normal to SPS CA (c-axis extension)	187	205	

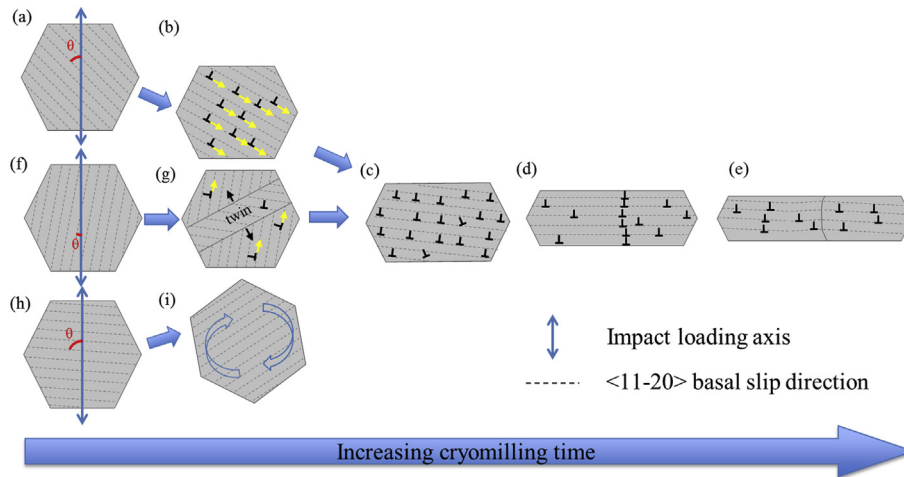


Fig. 10. A schematic showing the development of orientation preference and grain refinement in Mg during powder particle flattening.

shear stress is close to zero on the basal plane according to Schmid's law, due to the relatively low CRSS, basal slip can be activated under a small misalignment when θ_2 is not exactly zero.

Third, when compressed nearly perpendicular to the basal planes (Fig. 10 (h)), i.e., θ_3 is about 90° , contraction twins and $\langle c \rangle$ or $\langle c + a \rangle$ slips should be favored. However, due to the cryogenic environment, contraction twins and dislocation slip with $\langle c \rangle$ or $\langle c + a \rangle$ can only be activated under conditions that involve high stresses and/or strain rates, if material fracture does not occur prior to the activation of these modes. Therefore, this direction is considered as a hard direction on which inadequate strain can occur. Consequently, the particle will retain its initially equiaxed morphology, so the following impact direction relative to the crystal orientation could be arbitrary (Fig. 10 (i)) and possibly on soft directions, as in the first two scenarios. Particle fracture is also expected to occur readily under this loading condition. Similarly, some basal slip is expected when the Schmid factor for basal slip is not exactly zero.

As discussed in the first two scenarios, although a gradual lattice rotation by basal slip in the first scenario and an abrupt lattice reorientation induced by $\{10\text{--}12\}$ twinning in the second scenario, the c-axis of the crystal becomes closer to the impact loading axis during powder flattening, as shown in Fig. 10 (c). This is consistent with the crystal orientation preference observed in 2 h-Mg from the XRD results (Fig. 3). TEM results in Fig. 4 confirmed the relationship between powder flattening and the concomitant increase in density of basal $\langle a \rangle$ dislocations during 2 h of cryomilling. The high-density of basal dislocations then rearrange into subgrain boundaries perpendicular to the flattened lamellar surface (Fig. 10 (d)), and subgrain boundaries will continuously evolve into low or high angle grain boundaries

leading to refinement of the microstructure (Fig. 10 (e)).

4.2. Microstructural evolution during SPS consolidation

Despite the limited exposure time at elevated temperature during SPS, the microstructure of the AR-Mg-SPS reveals small equiaxed grains formed along the serrated coarse grain boundaries with a "necklace-like" grain structure (Fig. 5 (a)), which suggests the occurrence of dynamic recrystallization during SPS [34]. The presence of $30^\circ/[0001]$ grain boundaries (Fig. 8 (a)) is another feature that has been reported as an indicator of dynamic recrystallization in many thermo-mechanically processed Mg alloys [12,36]. Although the rotation axes for $\sim 30^\circ$ misorientation appears random for AR-Mg-SPS (Fig. 8 (a)), and shown again in Fig. 11 (a) for comparison), when the rotation axes distribution for $\sim 30^\circ$ misorientation is plotted with only small recrystallized grains (a $7 \mu\text{m}$ cutoff grain size is used), the IPF displays an obvious intensity peak around the c-axis, as displayed in Fig. 11 (b). A $7 \mu\text{m}$ grain size threshold is selected due to the first peak position in the grain size

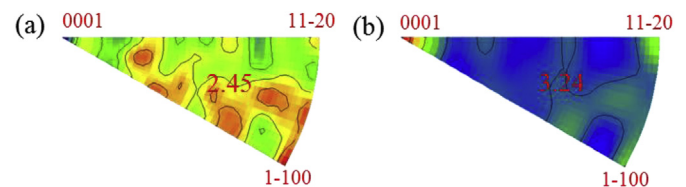


Fig. 11. Comparison of rotation axes distributions for grain boundaries with $(30 \pm 3)^\circ$ misorientation angles for AR-Mg-SPS when: (a) all grains are included and (b) only recrystallized grains (grains with diameters smaller than $7 \mu\text{m}$) are included.

histogram (Fig. 5 (c)). Therefore, owing to the small recrystallization fraction present in the AR-Mg-SPS, the frequency of $30^\circ/[0001]$ grain boundaries is low, and the overall misorientation distribution of the complete set of grains is observed to be random. In contrast, the notably higher frequency of $30^\circ/[0001]$ grain boundaries for 2 h-Mg-SPS suggests a higher fraction of recrystallized microstructure. In the SPS sintered Mg samples, the occurrence of dynamic recrystallization is feasible considering the 390°C sintering temperature, which exceeds the recrystallization temperature of Mg ($T_{RX} \approx 0.4T_m \approx 100^\circ\text{C}$). The 200 MPa uniaxial pressure applied to the Mg powder provides the major driving force for dynamic recrystallization in AR-Mg-SPS. In 2 h-Mg-SPS, however, the stored lattice energy due to a high dislocation density created during cryomilling can provide a higher driving force for recovery and recrystallization, resulting in a higher recrystallization fraction. Considering the low stacking fault energy (SFE) ($\sim 36\text{ mJ/m}^2$) on the basal planes and high SFEs on the non-basal planes ($\sim 265\text{ mJ/m}^2$ and $\sim 344\text{ mJ/m}^2$ for prismatic and pyramidal planes, respectively) [34], dislocations on the non-basal planes have a tendency to cross-slip onto the basal planes during dynamic recovery [34]. This is consistent with the TEM observation of cross-slipping dislocations in 2 h-Mg-SPS (Fig. 7 (c)).

Regarding texture evolution, both AR-Mg-SPS and 2 h-Mg-SPS did not show any deformation or recrystallization texture unique to SPS. Recrystallization is not effective in randomizing the texture, as noted in previous studies [44]. A basal fiber texture typical for wrought Mg and Mg alloys was observed in the SPS-consolidated samples. The basal texture being formed in AR-Mg-SPS without experiencing cryomilling can be attributed to the thermo-mechanical SPS process. The sharper texture in 2 h-Mg-SPS is a mixed result of the preferred crystal orientations in the disc-shaped cryomilled powder and the SPS thermo-mechanical effect.

4.3. Mechanisms for the reversed compressive yield strength anisotropy in 2 h-Mg-SPS

Generally, basal textured Mg exhibits a much lower yield strength upon c-axis extension compared to the yield strength upon c-axis contraction, because activating $\{10\text{--}12\}$ extension twinning is easy in the former but not favorable in the latter [6,45,46]. The yield strength for c-axis extension is usually one half to three quarters of that for c-axis contraction in polycrystalline Mg and Mg alloys with basal textures [9,47,48]. Compressive yield

strengths for the two SPS consolidated Mg samples, together with compressive data from the literature for textured commercially pure Mg [49] and dilute AZ31 Mg alloys [45,50,51] with equiaxed grain structure, are summarized in Fig. 12 as a function of average grain size. With decreasing grain size, the yield strength increases, as anticipated on the basis of the Hall-Petch relationship. However, for all the samples with equiaxed grain structure, the reduced grain size is not effective in reducing the compressive yield strength anisotropy. In contrast, both of the SPS sintered Mg samples display less anisotropic yield strength values, when compressed at room temperature. This can be partially explained by the weak texture in Mg processed via powder metallurgy. However, the difference in yield strength values for c-axis contraction and c-axis extension was further reduced in 2 h-Mg-SPS relative to AR-Mg-SPS, despite the stronger intensity of basal texture in 2 h-Mg-SPS. In the present study, we report for the first time a reversed yield strength anisotropy, i.e., the yield strength under c-axis extension being higher than that under c-axis contraction, in commercially pure Mg. Reversed yield strength tension/compression asymmetry has been previously observed in Mg-rare earth alloys and has been attributed to the interaction between dislocations and precipitates and solutes during deformation [52,53]. However, yield strength asymmetry and/or anisotropy in pure (including commercially pure) Mg and dilute Mg alloys without rare earth additions has not been previously observed. To study the deformation mechanisms leading to this unusual mechanical behavior, post-mortem EBSD analysis was performed on a 2 h-Mg-SPS sample compressed normal to the SPS CA, or c-axis extension mode, to $\sim 4\%$ true strain, at which point the test was interrupted. The EBSD IPF map after interrupted compression is shown in Fig. 13 (a). The grains were color-coded with respect to the compression axis, which is the vertical direction in the image. Grain boundary misorientation analysis in Fig. 13 (b) shows that the percent of grain boundaries satisfying $86^\circ \pm 5^\circ$ misorientation angles is $\sim 2.5\%$, compared to $\sim 1.0\%$ before the compression test. The rotation axes of $\sim 86^\circ$ grain boundaries are mostly around $\langle 11\text{--}20 \rangle$, correlating to $\{10\text{--}12\}$ twins. These grain boundaries were colored in white in Fig. 13 (a). The frequency of $\{10\text{--}12\}$ twinning is considerably lower in 2 h-Mg-SPS even though the loading direction is favorable for twinning. As discussed previously that the yield strength anisotropy of Mg is mainly due to the $\{10\text{--}12\}$ twinning, the smaller differential in compressive yield strengths observed in 2 h-Mg-SPS can be explained by the low occurrence of $\{10\text{--}12\}$ twinning.

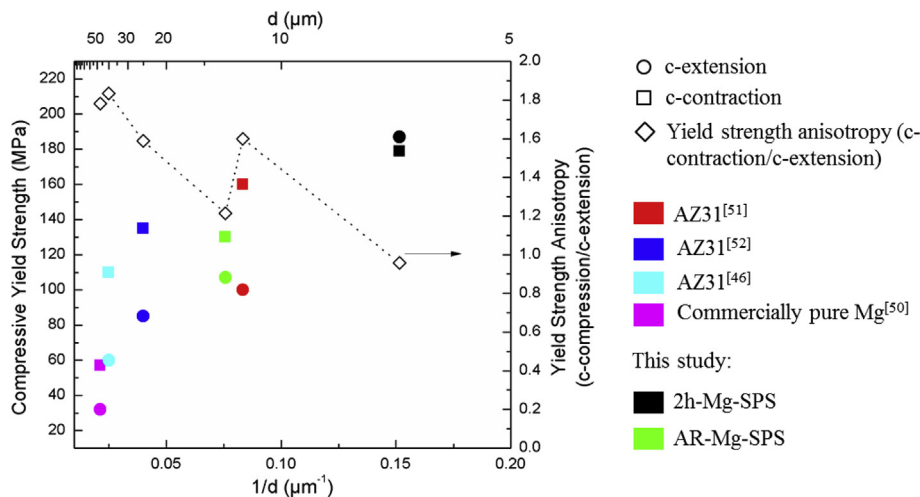


Fig. 12. Compressive yield strengths under c-axis compression and c-axis extension, and the yield strength anisotropy (c-contraction/c-extension) for Mg and dilute Mg alloys with different grain sizes.

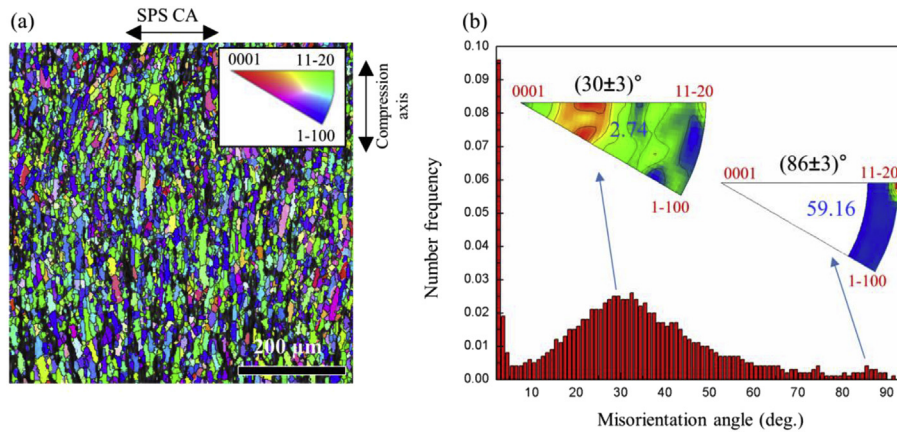


Fig. 13. Post-mortem EBSD microstructural analysis of 2 h-Mg-SPS compressed to ~4% true strain normal to SPS CA: (a) shows the IPF colored map, and (b) is the corresponding correlated misorientation angle distribution. Insets in (b) are the misorientation axis distributions for two angular ranges of interest.

The influence of grain size is likely related to the scarcity of twins in fine to ultrafine grained Mg. As extrapolated from the model derived by Barnett et al. for Mg alloys [47], the critical grain size for transition from twinning-dominated to slip-dominated deformation is less than $2\ \mu\text{m}$ at ambient temperature and quasi-static strain rate. The average equivalent spherical grain size in 2 h-Mg-SPS is $\sim 6.6\ \mu\text{m}$, which should fall in the twinning dominated regime. For example, in a hot rolled AZ31 with an average grain size of $8.1\ \mu\text{m}$, though the grain size is comparable to the average equivalent spherical grain size of 2 h-Mg-SPS, the yield strength for c-axis contraction is almost twice that for c-axis extension [54], indicating that the reduced grain size may not be the dominant mechanism for the reversed compressive yield strength anisotropy observed in 2 h-Mg-SPS. However, it should be pointed out that in the non-equiaxed microstructure of 2 h-Mg-

SPS, the average linear intercept grain size along the lamellar thickness direction is only $\sim 2.8\ \mu\text{m}$, which is close in value to the critical grain size for the suppression of twins. Further effort is still needed to explore the effects of different grain size parameters on the suppression of twin nucleation in polycrystalline Mg with non-equiaxed microstructures. In addition to twin nucleation, grain morphology may also influence the growth of twins. It is expected that the propagation and thickening of twins will be more difficult in 2 h-Mg-SPS compared to equivalent behavior observed in equiaxed grain structures with similar equivalent spherical grain sizes, because of the smaller dimensions along the lamellar thickness direction. For this reason, the grain morphology evidently affects the stress required for twin growth, which could contribute to the reversed yield anisotropy observed in the microlaminated 2 h-Mg-SPS.

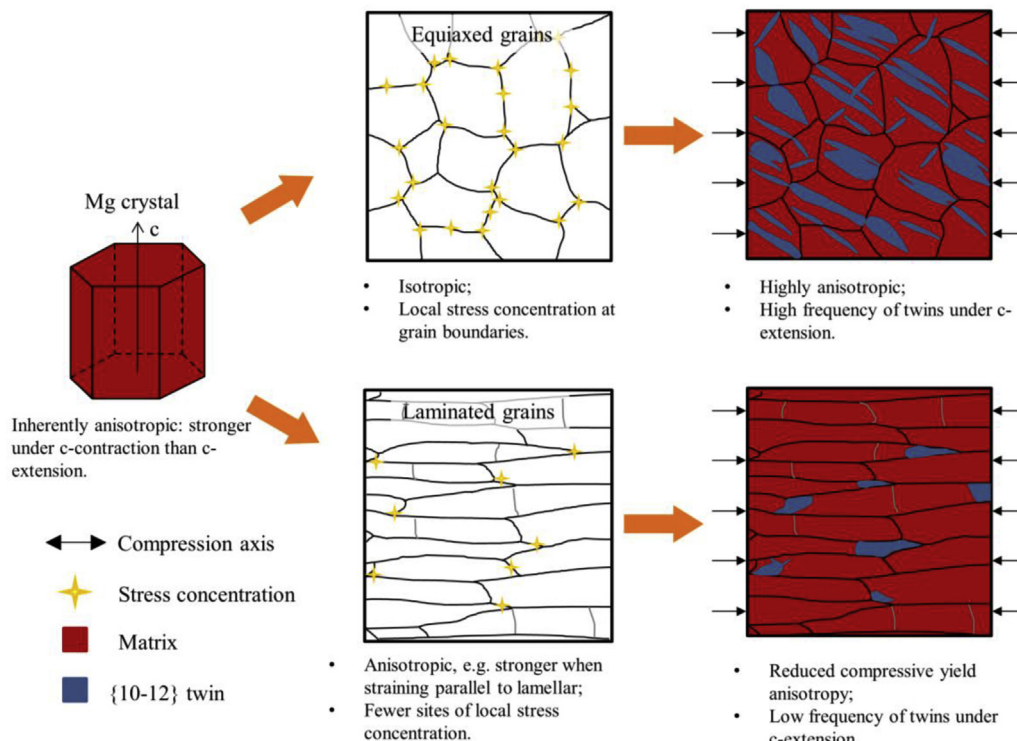


Fig. 14. Schematic showing the effects of equiaxial and laminated grain structure on the yield strength anisotropy of Mg.

As illustrated schematically in Fig. 14, Mg crystals show an intrinsically anisotropic mechanical behavior. An equiaxed grain structure, which usually induces isotropic properties in cubic materials with random textures, results in anisotropic compressive yield strength in textured Mg and profuse {10–12} twins can be activated at preferred stress orientations. In contrast, a laminated microstructure in cubic materials often leads to anisotropic properties for different loading orientations with respect to the lamellar planes, e.g., stronger when strained parallel to the lamellar plane [25]. However, it is proposed that the grain morphology induced deformation anisotropy observed in the present study offers an opportunity to reduce or even reverse the intrinsic compressive yield strength anisotropy of basal textured Mg. In addition, compared to an equiaxed structure with similar grain size, a laminated microstructure provides fewer sites for local stress concentration at grain boundaries that may facilitate twin nucleation, as seen in Fig. 14. Therefore, we attribute the reversed compressive yield strength anisotropy and low frequency of twins observed in 2 h-Mg-SPS to its microlaminated grain structure.

Another plausible explanation for the inhibition of twinning in 2 h-Mg-SPS is the high density of basal dislocations. As discussed in the previous sections, basal slip is dominant during cryomilling, and recovery on the basal plane with low stacking fault energy is difficult in Mg while non-basal dislocations tend to cross-slip onto basal planes during recovery. As a result, a high density of basal dislocations in both 2 h-Mg and 2 h-Mg-SPS was observed by TEM (Figs. 4 (b) and Fig. 7 (c)), which can considerably harden basal slip and decrease the CRSS ratio for non-basal to basal slip. Therefore, due to the more isotropic slip systems, the contribution of twinning in deformation could be reduced.

5. Conclusions

Mg with microlaminated grained structure was produced by cryomilling followed by consolidation using spark plasma sintering. Rigorous microstructural characterization was performed to explain the observed mechanical behavior. The following conclusions can be drawn from these analyses:

- 1 Particle-flattening occurred in the first 2 h of cryomilling. A high density of basal dislocations was introduced into the powder particles (2 h-Mg), together with a moderate amount of non-basal dislocations. The predominance of basal slip led to the formation of a preferred crystal orientation with the c-axis nearly perpendicular to the surface of the disc-shaped particles.
- 2 EBSD analyses indicate that after SPS consolidation, a basal fiber texture developed in samples starting with either the as-received powders (AR-Mg-SPS) or those after 2 h of cryomilling (2 h-Mg-SPS). The stronger texture in 2 h-Mg-SPS is attributed to the preferential orientations developed in the disc-shaped particles and the thermo-mechanical effect of SPS. Dynamic recovery and recrystallization also occurred and promoted dislocation cross-slipping.
- 3 2 h-Mg-SPS achieves higher compression yield strengths than AR-Mg-SPS under both c-axis contraction and c-axis extension. Though AR-Mg-SPS exhibits a compressive yield anisotropy linked with its basal texture, a reversed compressive yield anisotropy was observed in 2 h-Mg-SPS, with a low occurrence of twinning activity during compression normal to the basal pole.
4. The low twinning activity, limited growth of twins and the anisotropy induced by the laminated grain structure are important contributors to the reversed yield anisotropy in 2 h-Mg-SPS.

Acknowledgements

This work was supported by the National Science Foundation (NSF CMMI-1631873 and NSF CMMI-1729887). Dr. Baolong Zheng's assistance with cryomilling is greatly appreciated.

References

- [1] W.J. Joost, Targeting high impact R&D for automotive magnesium alloys, in: K.N. Solanki, D. Orlov, A. Singh, N.R. Neelamegham (Eds.), *Magnesium Technology 2017*, Springer International Publishing, Cham, 2017, pp. 5–6.
- [2] C. Bettles, M. Gibson, Current wrought magnesium alloys: strengths and weaknesses, *JOM* 57 (5) (2005) 46–49.
- [3] W.B. Hutchinson, M.R. Barnett, Effective values of critical resolved shear stress for slip in polycrystalline magnesium and other hcp metals, *Scr. Mater.* 63 (7) (2010) 737–740.
- [4] S.R. Agnew, O. Duygulu, Plastic anisotropy and the role of non-basal slip in magnesium alloy AZ31B, *Int. J. Plast.* 21 (6) (2005) 1161–1193.
- [5] J.P. Hirth, J. Lothe, *Theory of Dislocations*, McGraw-Hill, 1967.
- [6] A. Styczynski, C. Hartig, J. Bohlen, D. Letzig, Cold rolling textures in AZ31 wrought magnesium alloy, *Scr. Mater.* 50 (7) (2004) 943–947.
- [7] M.R. Barnett, M.D. Nave, C.J. Bettles, Deformation microstructures and textures of some cold rolled Mg alloys, *Mater. Sci. Eng.* 386 (1–2) (2004) 205–211.
- [8] Y.N. Wang, J.C. Huang, Texture analysis in hexagonal materials, *Mater. Chem. Phys.* 81 (1) (2003) 11–26.
- [9] S.R. Agnew, M.H. Yoo, C.N. Tomé, Application of texture simulation to understanding mechanical behavior of Mg and solid solution alloys containing Li or Y, *Acta Mater.* 49 (20) (2001) 4277–4289.
- [10] D. Zhang, H. Wen, M.A. Kumar, F. Chen, L. Zhang, I.J. Beyerlein, J.M. Schoenung, S. Mahajan, E.J. Lavernia, Yield symmetry and reduced strength differential in Mg-2.5Y alloy, *Acta Mater.* 120 (2016) 75–85.
- [11] T. Al-Samman, X. Li, Sheet texture modification in magnesium-based alloys by selective rare earth alloying, *Mater. Sci. Eng.* 528 (10–11) (2011) 3809–3822.
- [12] J. Hirsch, T. Al-Samman, Superior light metals by texture engineering: optimized aluminum and magnesium alloys for automotive applications, *Acta Mater.* 61 (3) (2013) 818–843.
- [13] I.J. Beyerlein, L.S. Toth, Texture evolution in equal-channel angular extrusion, *Prog. Mater. Sci.* 54 (4) (2009) 427–510.
- [14] J. Bohlen, M.R. Nürnberg, J.W. Senn, D. Letzig, S.R. Agnew, The texture and anisotropy of magnesium–zinc–rare earth alloy sheets, *Acta Mater.* 55 (6) (2007) 2101–2112.
- [15] J.A. Yasi, L.G. Hector Jr., D.R. Trinkle, Prediction of thermal cross-slip stress in magnesium alloys from a geometric interaction model, *Acta Mater.* 60 (5) (2012) 2350–2358.
- [16] C.M. Cepeda-Jiménez, J.M. Molina-Aldareguia, M.T. Pérez-Prado, Origin of the twinning to slip transition with grain size refinement, with decreasing strain rate and with increasing temperature in magnesium, *Acta Mater.* 88 (2015) 232–244.
- [17] C.M. Cepeda-Jiménez, J.M. Molina-Aldareguia, F. Carreño, M.T. Pérez-Prado, Prominent role of basal slip during high-temperature deformation of pure Mg polycrystals, *Acta Mater.* 85 (2015) 1–13.
- [18] Q. Yu, L. Qi, R.K. Mishra, J. Li, A.M. Minor, Reducing deformation anisotropy to achieve ultrahigh strength and ductility in Mg at the nanoscale, *Proc. Natl. Acad. Sci. U.S.A.* 110 (33) (2013) 13289–13293.
- [19] D.B. Witkin, E.J. Lavernia, Synthesis and mechanical behavior of nanostructured materials via cryomilling, *Prog. Mater. Sci.* 51 (1) (2006) 1–60.
- [20] C. Suryanarayana, Mechanical alloying and milling, *Prog. Mater. Sci.* 46 (1–2) (2001) 1–184.
- [21] C.C. Koch, Synthesis of nanostructured materials by mechanical milling: problems and opportunities, *Nanostruct. Mater.* 9 (1) (1997) 13–22.
- [22] Z. Li, Q. Guo, Z. Li, G. Fan, D.-B. Xiong, Y. Su, J. Zhang, D. Zhang, Enhanced mechanical properties of graphene (reduced graphene oxide)/aluminum composites with a bio-inspired nanolaminated structure, *Nano Lett.* 15 (12) (2015) 8077–8083.
- [23] L. Jiang, Z. Li, G. Fan, L. Cao, D. Zhang, The use of flake powder metallurgy to produce carbon nanotube (CNT)/aluminum composites with a homogenous CNT distribution, *Carbon* 50 (5) (2012) 1993–1998.
- [24] L. Jiang, Z. Li, G. Fan, L. Cao, D. Zhang, Strong and ductile carbon nanotube/aluminum bulk nanolaminated composites with two-dimensional alignment of carbon nanotubes, *Scr. Mater.* 66 (6) (2012) 331–334.
- [25] S. Feng, Q. Guo, Z. Li, G. Fan, Z. Li, D.-B. Xiong, Y. Su, Z. Tan, J. Zhang, D. Zhang, Strengthening and toughening mechanisms in graphene-Al nanolaminated composite micro-pillars, *Acta Mater.* 125 (2017) 98–108.
- [26] M. Pozuelo, C. Melnyk, W.H. Kao, J.-M. Yang, Cryomilling and spark plasma sintering of nanocrystalline magnesium-based alloy, *J. Mater. Res.* 26 (07) (2011) 904–911.
- [27] B.L. Zheng, O. Ertorer, Y. Li, Y.Z. Zhou, S.N. Mathaudhu, C.Y.A. Tsao, E.J. Lavernia, High strength, nano-structured Mg–Al–Zn alloy, *Mater. Sci. Eng.* 528 (4–5) (2011) 2180–2191.
- [28] A. Levinson, R.K. Mishra, R.D. Doherty, S.R. Kalidindi, Influence of deformation twinning on static annealing of AZ31 Mg alloy, *Acta Mater.* 61 (16) (2013) 5966–5978.

- [29] S. Zheng, I.J. Beyerlein, J.S. Carpenter, K. Kang, J. Wang, W. Han, N.A. Mara, High-strength and thermally stable bulk nanolayered composites due to twin-induced interfaces, *Nat. Commun.* 4 (2013) 1696.
- [30] D.A. Hughes, N. Hansen, Microstructure and strength of nickel at large strains, *Acta Mater.* 48 (11) (2000) 2985–3004.
- [31] B. Beausir, S. Biswas, D.I. Kim, L.S. Tóth, S. Suwas, Analysis of microstructure and texture evolution in pure magnesium during symmetric and asymmetric rolling, *Acta Mater.* 57 (17) (2009) 5061–5077.
- [32] Z.R. Zeng, M.Z. Bian, S.W. Xu, C.H.J. Davies, N. Birbilis, J.F. Nie, Texture evolution during cold rolling of dilute Mg alloys, *Scr. Mater.* 108 (2015) 6–10.
- [33] S. Sandlöbes, S. Zaeferrer, I. Schectakow, S. Yi, R. Gonzalez-Martinez, On the role of non-basal deformation mechanisms for the ductility of Mg and Mg–Y alloys, *Acta Mater.* 59 (2) (2011) 429–439.
- [34] S. Biswas, S. Singh Dhinwal, S. Suwas, Room-temperature equal channel angular extrusion of pure magnesium, *Acta Mater.* 58 (9) (2010) 3247–3261.
- [35] N. Dixit, K.Y. Xie, K.J. Hemker, K.T. Ramesh, Microstructural evolution of pure magnesium under high strain rate loading, *Acta Mater.* 87 (2015) 56–67.
- [36] B. Li, M. Liao, Q. Ma, Z. McClelland, Structure of grain boundaries with $30^\circ[0\ 0\ 1]$ misorientation in dynamically recrystallized magnesium alloys, *Comput. Mater. Sci.* 101 (2015) 175–180.
- [37] J.C. Tan, M.J. Tan, Dynamic continuous recrystallization characteristics in two stage deformation of Mg–3Al–1Zn alloy sheet, *Mater. Sci. Eng.* 339 (1) (2003) 124–132.
- [38] M. Knezevic, A. Levinson, R. Harris, R.K. Mishra, R.D. Doherty, S.R. Kalidindi, Deformation twinning in AZ31: influence on strain hardening and texture evolution, *Acta Mater.* 58 (19) (2010) 6230–6242.
- [39] T. Al-Samman, K.D. Molodov, D.A. Molodov, G. Gottstein, S. Suwas, Softening and dynamic recrystallization in magnesium single crystals during c-axis compression, *Acta Mater.* 60 (2) (2012) 537–545.
- [40] E.J. Lavernia, B.Q. Han, J.M. Schoenung, Cryomilled nanostructured materials: processing and properties, *Mater. Sci. Eng.* 493 (1–2) (2008) 207–214.
- [41] J.S. Benjamin, T.E. Volin, The mechanism of mechanical alloying, *Met. Trans.* 5 (8) (1974) 1929–1934.
- [42] F. Zhou, X.Z. Liao, Y.T. Zhu, S. Dallek, E.J. Lavernia, Microstructural evolution during recovery and recrystallization of a nanocrystalline Al–Mg alloy prepared by cryogenic ball milling, *Acta Mater.* 51 (10) (2003) 2777–2791.
- [43] B. Zheng, O. Ertozer, Y. Li, Y. Zhou, S.N. Mathaudhu, C.Y.A. Tsao, E.J. Lavernia, High strength, nano-structured Mg–Al–Zn alloy, *Mater. Sci. Eng.* 528 (4–5) (2011) 2180–2191.
- [44] R. Cottam, J. Robson, G. Lorimer, B. Davis, Dynamic recrystallization of Mg and Mg–Y alloys: crystallographic texture development, *Mater. Sci. Eng.* 485 (1–2) (2008) 375–382.
- [45] A.S. Khan, A. Pandey, T. Gnäupel-Herold, R.K. Mishra, Mechanical response and texture evolution of AZ31 alloy at large strains for different strain rates and temperatures, *Int. J. Plast.* 27 (5) (2011) 688–706.
- [46] M.H. Yoo, Slip, twinning, and fracture in hexagonal close-packed metals, *Metall. Trans. A* 12 (3) (1981) 409–418.
- [47] M.R. Barnett, Z. Keshavarz, A.G. Beer, D. Atwell, Influence of grain size on the compressive deformation of wrought Mg–3Al–1Zn, *Acta Mater.* 52 (17) (2004) 5093–5103.
- [48] H. Yu, Y. Xin, A. Chapuis, X. Huang, R. Xin, Q. Liu, The different effects of twin boundary and grain boundary on reducing tension-compression yield asymmetry of Mg alloys, *Sci. Rep.* 6 (2016), 29283.
- [49] M.D. Nave, M.R. Barnett, Microstructures and textures of pure magnesium deformed in plane-strain compression, *Scr. Mater.* 51 (9) (2004) 881–885.
- [50] E. Yukutake, J. Kaneko, M. Sugamata, Anisotropy and non-uniformity in plastic behavior of AZ31 magnesium alloy plates, *Mater. Trans.* 44 (4) (2003) 452–457.
- [51] B. Wang, R. Xin, G. Huang, Q. Liu, Effect of crystal orientation on the mechanical properties and strain hardening behavior of magnesium alloy AZ31 during uniaxial compression, *Mater. Sci. Eng.* 534 (2012) 588–593.
- [52] P. Hidalgo-Manrique, J.D. Robson, M.T. Pérez-Prado, Precipitation strengthening and reversed yield stress asymmetry in Mg alloys containing rare-earth elements: a quantitative study, *Acta Mater.* 124 (2017) 456–467.
- [53] P. Hidalgo-Manrique, V. Herrera-Solaz, J. Segurado, J. Llorca, F. Gálvez, O.A. Ruano, S.B. Yi, M.T. Pérez-Prado, Origin of the reversed yield asymmetry in Mg-rare earth alloys at high temperature, *Acta Mater.* 92 (2015) 265–277.
- [54] S.H. Park, J.H. Lee, B.G. Moon, B.S. You, Tension–compression yield asymmetry in as-cast magnesium alloy, *J. Alloy. Comp.* 617 (2014) 277–280.